

The International Journal of Robotics Research

<http://ijr.sagepub.com/>

Undulatory swimming in sand: experimental and simulation studies of a robotic sandfish

Ryan D Maladen, Yang Ding, Paul B Umbanhowar and Daniel I Goldman

The International Journal of Robotics Research 2011 30: 793 originally published online 3 June 2011

DOI: 10.1177/0278364911402406

The online version of this article can be found at:

<http://ijr.sagepub.com/content/30/7/793>

Published by:



<http://www.sagepublications.com>

On behalf of:



Multimedia Archives

Additional services and information for *The International Journal of Robotics Research* can be found at:

Email Alerts: <http://ijr.sagepub.com/cgi/alerts>

Subscriptions: <http://ijr.sagepub.com/subscriptions>

Reprints: <http://www.sagepub.com/journalsReprints.nav>

Permissions: <http://www.sagepub.com/journalsPermissions.nav>

Citations: <http://ijr.sagepub.com/content/30/7/793.refs.html>

Undulatory swimming in sand: experimental and simulation studies of a robotic sandfish

Ryan D Maladen¹, Yang Ding², Paul B Umbanhowar³ and Daniel I Goldman^{1,2}

Abstract

A previous study of a sand-swimming lizard, the sandfish, revealed that it swims within granular media at speeds up to 0.4 body-lengths/cycle using body undulations (approximately a single period sinusoidal traveling wave) without limb use. Inspired by the organism, we develop a numerical model of a robot swimming in a simulated granular medium to guide the design of a physical device. Both in simulation and experiment the robot swims limlessly subsurface at speeds up to 0.3 body-lengths/cycle and, like the animal, increases its speed by increasing its oscillation frequency. The performance of the robot measured in terms of its wave efficiency η , the ratio of its forward speed to wave speed, is 0.34 ± 0.02 , within 8% of the simulation prediction. Both in simulation and experiment, η increases with increasing particle–particle friction but decreases with increasing body–particle friction. On a flat, rigid surface the robot fails to move forward, as expected, due to the frictional isotropy between the interacting surfaces. However, the surface and subsurface performance of the robot on low friction particles are comparable. Our work provides a validated simulation tool and the design of a robot that can move on or within yielding terrestrial substrates.

Keywords

Bioinspired, swimming, sand, limbless, modeling, subsurface

1. Introduction

There is a need for robots that move on and within complex material such as sand, rubble, and loose debris. For example, such robots could locate hazardous chemical leaks (Humphrey and Adams 2009), function as self-propelled inspection devices (McKean et al. 1991), and search for victims in disaster sites (Ashcheulov et al. 2000; Marcus et al. 2003; Metternicht et al. 2005). Limbless robots that use their bodies to move through material appear best suited to navigate these terrains since traditional wheeled (Wong 1984; Siegwart et al. 2002; Arena et al. 2004; Ritzmann et al. 2004) and legged robots (Saranli et al. 2001; Kim et al. 2006; Playter et al. 2006; Saunders et al. 2006; Hoover et al. 2008; Li et al. 2009, 2010) are often impeded by their appendages which can result in entrapment and failure.

Snake-inspired robots were introduced in the 1970s by Hirose et al. (1993) and most subsequent designs of limbless robots have followed the theme of mimicking snake locomotion, but have differed greatly in physical configuration and purpose (Hopkins et al. 2009). Snake robots that use lateral undulations to locomote do so by mimicking the anisotropy in lateral and longitudinal friction coefficients in the scale structure on the ventral surface of snakes which

allows them to progress forward (Hu et al. 2009). This anisotropy is achieved by attaching small wheels (active or passive) to each segment, which results in a low friction coefficient in the forward direction and a high coefficient in the lateral direction. The segments are connected by motors and the angles between adjacent segments controlled to enable locomotion by propagating a traveling wave along the body of the robot (Hirose et al. 1993; Crespi et al. 2005; Ijspeert et al. 2007). Most of these serpentine robots have been tested on rigid surfaces (Hirose and Morishima 1990; Shan and Koren 1993; Desai et al. 1995; Klaassen and Paap 1999) while only a few have been developed for and tested in unstructured environments (Hirose et al. 1993;

¹Bioengineering Program, Georgia Institute of Technology, Atlanta, GA, USA

²School of Physics, Georgia Institute of Technology, Atlanta, GA, USA

³Department of Mechanical Engineering, Northwestern University, Evanston, IL, USA

Corresponding author:

Daniel I Goldman, Bioengineering Program and School of Physics, Georgia Institute of Technology, 837 State Street, Atlanta, GA 30332-0250, USA

Email: daniel.goldman@physics.gatech.edu

Chirikjian and Burdick 1995; Dowling 1999; Choset et al. 2000; Crespi et al. 2005).

Advances in creating high-performing flying and swimming devices (Kim et al. 2002; Crespi et al. 2005; Zuferey et al. 2007) in aerial and aquatic domains, and wheeled/tracked vehicles on relatively structured terrestrial terrain have occurred mainly because the respective fields of aerodynamics, fluid dynamics, and terramechanics (Bekker 1956; Kim et al. 2002) provide accurate models of locomotor-media interaction which are in turn used to design improved wings, fins, and wheels. However, a major hurdle arises when designing robots to move on and within complex flowing particulate environments (e.g. sand, soil, and leaf-litter) that can display both solid- and fluid-like behavior in response to stress. In such materials, the physics of penetration and drag is largely unexplored for realistic conditions, and comparable comprehensive validated analytic continuum theories at the level of the Navier-Stokes equations (Tritton 1989) for fluids do not exist. However, it is possible to understand the interaction between the locomotor and the media using numerical and physical modeling approaches (Gerritsen et al. 1995; Mouazen and Nemenyi 1999; Rapaport 2004).

In the absence of validated theory, the biological world is a fruitful source of principles of locomotion that can be incorporated into robots designed to move within complex substrates. Many desert organisms like scorpions, snakes, and lizards burrow and swim effectively in sand (Hawke and Farley 1973; Fielden 1991; Seymour et al. 2001; Meysman et al. 2006; Dorgan et al. 2007) to escape from heat and predators, and to hunt for prey (Arnold 1995; White 2003). It has been hypothesized that these animals have evolved morphological adaptations such as body elongation and limb reduction to deal with deformable terrain (Gans 1975; Carranza et al. 2008). Our recent high-speed X-ray imaging study investigating the subsurface locomotion of the sandfish *Scincus scincus*, a small (~10 cm from snout to tail tip) desert-dwelling lizard that inhabits the Saharan desert (Maladen et al. 2009) (Figure 1), revealed that within the media the animal 'swims' forward by propagating a sinusoidal traveling wave posteriorly from head to tail without using its limbs.

Motivated by the subsurface locomotion of the sandfish, the present work utilizes a numerical simulation of a sandfish inspired undulator as a design tool to build an appendage-less sand-swimming device. The robot is driven by an open-loop controller which, like the animal kinematics, varies the joint position trajectories to create a sinusoidal wave that travels posteriorly along the device. The robot swims within a model laboratory granular medium of spherical plastic particles and displays locomotion features predicted by the numerical robot simulation and similar to those of the organism. We also utilize our sand-swimming robot to investigate whether the lateral undulation mechanism is effective for moving on the surface of granular media.

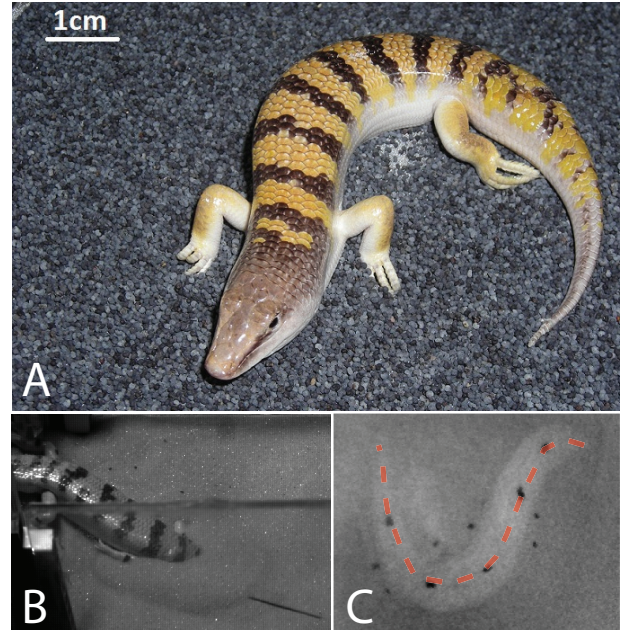


Fig. 1. (A) The sandfish *Scincus scincus*, a sand-swimming lizard that inhabits the Saharan desert, (B) burying into granular media (0.27 ± 0.04 mm diameter approximately spherical glass particles), and (C) swimming subsurface where the X-ray image shows the body (light area) and opaque markers fixed to limbs and midline. Red dashed line indicates tracked midline.

2. Previous work

2.1. Biological experiment

The biological experiments of Maladen et al. (2009) modeled the subsurface undulatory motion of the sandfish with a posteriorly traveling single-period sinusoidal wave

$$y = A \sin \frac{2\pi}{\lambda}(x + v_w t) \quad (1)$$

with x the position along the sandfish midline, y the body displacement from the midline, A the amplitude, λ the wavelength and $v_w = f\lambda$ the wave speed where f is the oscillation frequency. The spatial characteristics, A and λ , did not vary significantly with media preparation and their ratio was fixed at ≈ 0.2 implying that the animal increased its forward velocity by increasing its oscillation frequency.

While swimming in a deformable medium undulatory swimmers across scales (e.g. spermatozoa and eels in fluids) (Gray and Hancock 1955; Gray and Lissmann 1964; Gillis 1996) progress a distance that is less than their wavelength per cycle of undulation. The reduced performance is referred to as 'slip' and can be characterized by the wave efficiency ($\eta = 1 - \text{slip}$), the ratio of the average forward speed of the animal, v_x , to the velocity of the wave traveling down its body, v_w , or equivalently the slope of the velocity-frequency relationship for velocity measured in

wavelengths per second. Typical wave efficiencies of undulatory organisms moving in fluids at low Reynolds number (such as nematodes in water) are 0.25 (Gray and Hancock 1955; Berri et al. 2009; Cohen and Boyle 2010), whereas $\eta \approx 0.8$ – 0.9 for organisms undulating (creeping) along the solid–air interfaces (Gray 1946; Gray and Lissmann 1964; Jayne 1986). Locomotion with $\eta = 1$ is equivalent to moving within a rigid tube such that all points along the body axis follow the same trajectory as the undulatory wave. For the sandfish swimming in glass particles, $\eta \approx 0.5$ independent of particle size and packing density (Maladen et al. 2009).

2.2. Resistive force theory for granular media

An empirical resistive force theory (RFT) was developed to predict wave efficiency η for undulatory subsurface granular locomotion (Maladen et al. 2009). The RFT, inspired by theory used to predict swimming speeds of microorganisms in fluids (Gray and Hancock 1955), partitions the body of the organism into infinitesimal segments each of which generates thrust and experiences drag when moving through a granular medium. These segmental forces are integrated over the entire body, and, by setting the net forward force to zero (assuming a constant average velocity), η is obtained numerically.

Unlike fluids, in granular media no validated theory exists in the velocity regime relevant to sand-swimming to estimate the force on individual segments. Previously, Maladen et al. (2009) obtained these forces empirically by dragging a rod (representative segment) through the media the animal was tested in. With these forces as input and by propagating a sinusoidal traveling wave along the body, the RFT shows that translational motion within granular media without limb use is possible. Also, the RFT accurately predicts that the sandfish swims with $\eta \approx 0.5$ within a granular media of 0.27 ± 0.04 mm diameter spherical glass particles (representative in size to desert sand) (Bagnold 1954).

While RFT qualitatively describes some features of sand-swimming, it is based on several assumptions, e.g. the measured drag force on a rod is representative of the average force on a segment of the sandfish, the forces generated by a segment are localized, and the center of mass of the animal does not oscillate laterally. Since the assumptions of the RFT have not been rigorously tested and applying RFT to different treatments (particle friction, particle size, body morphology, etc.) requires force laws to be measured for each condition, we instead use numerical simulation techniques as a general robotic design tool.

A numerical simulation approach, once validated against experiment, can provide an understanding of body generated drag and thrust forces at the particle scale and can be used to generate empirical drag laws for input into RFT. Our numerical simulation is a flexible design tool that accurately predicts robot performance and allows easy variation of physical and design parameters such as friction and number of robot segments.

3. Numerical simulation of a sand-swimming robot

3.1. Development and validation

To design a sand-swimming robot, we developed a numerical simulation of a laboratory scale device with a finite number of discrete, rigid segments to test whether it could swim within granular media. The simulation couples a numerical model of the robot to a model of the granular medium. We simulate the granular material using 3D discrete element method (DEM) (Rapaport 2004) simulation. To compute the robot–particle and particle–particle interaction forces we calculate the normal force (Lee and Herrmann 1993), F_n , and the Coulombic tangential force, F_s , at each contact with

$$\begin{aligned} F_n &= k\delta^{3/2} - G_n v_n \delta^{1/2}, \\ F_s &= \mu F_n, \end{aligned} \quad (2)$$

where δ is the virtual overlap between particles or between particle and robot segment, v_n is the normal component of relative velocity, and k and G_n are the hardness and viscoelastic constant. μ quantifies the particle–particle (μ_{pp}) or body–particle (μ_{bp}) friction coefficient depending on which elements are in contact; values are given in Table 1. Here μ_{bp} was measured between the robot skin and plastic particles used in the physical experiments (see Section 4). To reduce the required torque in the physical experiments and to decrease the computational time, we used a granular medium composed of spherical plastic particles with diameter 5.87 ± 0.06 mm and density 1.03 ± 0.04 g cm⁻³ in experiment. In the simulation, the medium is a 50:50 bi-disperse mixture of 5.81 mm and 5.93 mm diameter particles with density 1.06 g cm⁻³. The 35 and 24 particle deep bed of particles was held in a 188 × 62 particle diameter container in experiment and simulation, respectively. To validate the simulated medium and obtain the values of μ_{pp} , k , and G_n given above, we dropped an aluminum ball (diameter 6.35 cm and mass 385 g) into the plastic particles with varying impact velocity (0.5–3 m s⁻¹) in both experiment and simulation and set grain interaction parameters to best match the measured and simulated penetration force during the impact collision as a function of time (Figure 2). With parameters determined from impact at $v = 1.4$ m s⁻¹, the force profile fit well at other impact velocities. In additional experiments, we directly measured μ_{pp} and the coefficient of restitution (determined by G_n with fixed k) for the plastic particles and found them to be within 5% and 10% of the fitted values respectively (see Table 1). For simplicity we used the same normal force parameters for both the particle–particle and body–particle interactions. Like other DEM simulation studies of granular media (Pica Ciarrarra et al. 2003; Silbert et al. 2001), we used k values smaller than the physical values in simulation to reduce the computational time. In our impact simulation, increasing k by 8 times while keeping the same restitution coefficient

Table 1. Properties of 6 mm diameter plastic particles PD is the average particle diameter of 5.87 mm.

	Experiment	Simulation
Hardness (k) ($\text{kg s}^{-2} \text{m}^{-1/2}$)	1.7×10^8	2×10^5
Restitution coefficient	0.96	0.88
G_n ($\text{kg m}^{-1/2} \text{s}^{-1}$)	1×10^2	5
$\mu_{\text{particle-particle}}$	0.073	0.080
$\mu_{\text{particle-body}}$	0.27	0.27
Density (g cm^{-3})	1.03 ± 0.04	1.06
Diameter	$5.87 \pm 0.06 \text{ mm}$	5.81 mm (50%) and 5.93 mm (50%)
Granular volume	188 PD \times 62 PD \times 35 PD	188 PD \times 62 PD \times 24 PD

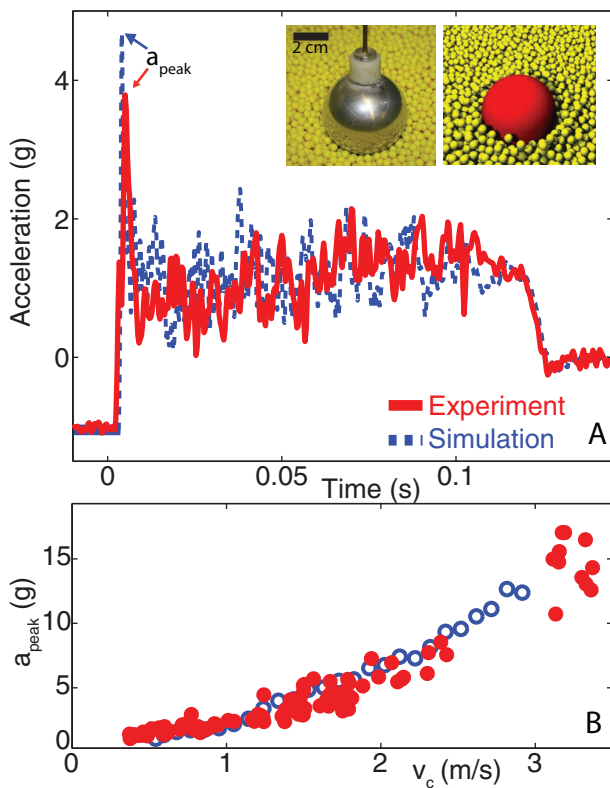


Fig. 2. Validating the numerical simulation for 6 mm diameter plastic spheres using the measured acceleration of a sphere during impact after free-fall (Goldman and Umbanhowar 2008). (a) Acceleration versus time in simulation (blue dashed trace) and experiment (red solid trace) with impact velocity of 1.4 m s^{-1} for a representative run. Acceleration is given in units of g , the acceleration due to gravity. (Left inset) Aluminum ball instrumented with accelerometer resting on 6 mm diameter plastic spheres. (Right inset) Ball and particles in simulation. (b) The peak acceleration during impact as function of impact velocity from simulation (blue open circles) and experiment (red filled circles).

times resulted in a qualitative match in the acceleration profiles.

To model the sand-swimming device we used a commercial multi-body simulator software package Working Model

(WM) 2D (Design Simulation Technologies). Modeling the device in a 2D simulation environment is sufficient to capture the dynamics since the sand-swimming robot moves roughly in a plane in this study. We also assume that the robot swims at a fixed depth although it rises slowly as it progresses forward due to drag-induced granular lift. This lift results from the vertical component of the normal force on an inclined surface dragged through a granular medium and is discussed in Ding et al. (2011) and Maladen et al. (2011b). The simulated robot was sized for easy testing of the corresponding physical device at the laboratory scale. Since the sandfish does not use its limbs to move subsurface and RFT has shown that body undulation is sufficient for propulsion (Maladen et al. 2009), the simulated robot is limbless. Unlike the sandfish, the device is not tapered. The simulated robot consists of 49 elements interconnected and actuated by virtual motors (vertical cylinders) of the same height (Figure 3). Depending on the number of segments (N) employed, every $48/N$ motor is driven with an open-loop signal to generate a sinusoidal wave traveling posteriorly from head to tail while the remaining motors (elements) are not actuated (immobilized) to form a straight segment. To approximate a sinusoidal traveling wave, the angle between adjacent segments is modulated using

$$\beta(i, t) = \beta_0 \xi \sin(2\pi \xi i/N - 2\pi ft), \quad (3)$$

where $\beta(i, t)$ is the motor angle of the i th actuated motor at time t , β_0 is the angular amplitude which determines A/λ , ξ the number of wavelengths along the body (period), and N the number of motors.

WM integrates the equations of motion of the coupled segments and the DEM calculates the resultant force from both particle-particle and body-particle interactions. For each time step, the net force from particles on each segment is passed to WM, and velocity and position information transferred back to DEM. Rotation about the axis of the traveling wave (roll and pitch) is not modeled.

Using Equation (3) the simulated robot with seven total segments moved forward within 6 mm diameter plastic particles and increased its forward speed linearly with oscillation frequency (Figure 4). The wave efficiency was $\eta = 0.36 \pm 0.02$, less than that of the sandfish lizard

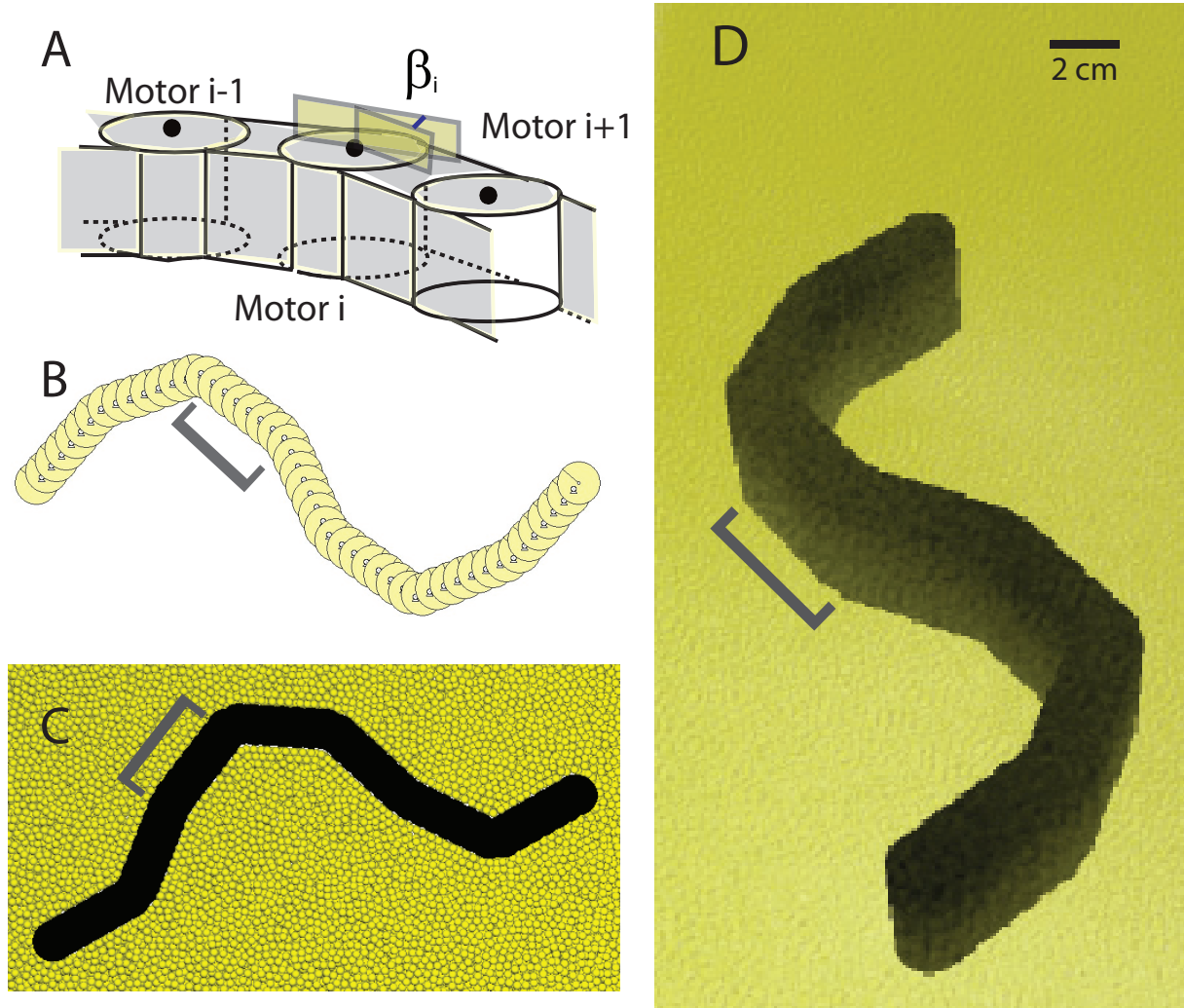


Fig. 3. Simulation of a sand-swimming robot. (A,B) Side and top view of the robot modeled with 49 inter-connected elements. For the 7 segment device shown, only every 8th element is actuated by a motor while all other motors are immobilized. The angle between adjacent actuated motors (β_i) is modulated according to Equation (3) to approximate the sandfish's sinusoidal traveling wave kinematics ($i = 1$ refers to the head). (C) Top view of the device submerged in 6 mm particles with particles above the robot rendered transparent. (D) Rendering of the simulated robot for the same parameters used in the robot experiment (see Figure 5). Grey brackets ([]) indicate a single robot segment of the seven segment robot.

($\eta \approx 0.5$). To test whether particle density had an effect on performance we tested the simulated robot within granular media with density 1.5 g cm^{-3} and 2.5 g cm^{-3} (glass particles used in the animal experiment (Maladen et al. 2009)) and found that η increased by 6% and 10%, respectively, as compared with performance within particles with density 1.06 g cm^{-3} . These results motivated us to build a physical instantiation of the simulated robot.

4. Sand-swimming robot

4.1. Design and control

The basic mechanical design of our device is adapted from previously developed snake robots (Dowling 1999) which

consist of repeated modules (motors) each with a single joint that permits angular excursions in a plane and connected via identical links. In our design, each module houses a servomotor attached to an aluminum bracket and connected to adjacent motors via aluminum connectors. The wire bundle that routes power and control signals to each motor is run atop each module over the length of the device and strain relieved at the last (tail) segment. For convenience and to maintain a reasonable size, our device employs six standard size servomotors and a dummy segment (the head) with the same weight and form factor as the motor segments for a total of seven segments (Figure 5A).

Simulation of the physical device found that the peak torque required to swim subsurface at a depth of 4 cm

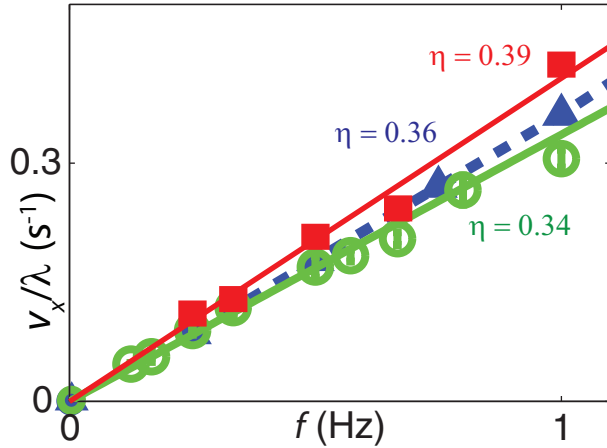


Fig. 4. Forward velocity versus oscillation frequency relationship for the robot subsurface in experiment (green circles) and in simulation (blue triangles), and on the surface (red squares) in experiment ($A/\lambda = 0.2$ and $\xi = 1$). The slope of the dashed blue (subsurface simulation), solid green (subsurface experiment), and red solid (surface experiment) fit lines give wave efficiencies η of 0.36 ± 0.02 , 0.34 ± 0.02 , and 0.39 ± 0.02 , respectively. The granular medium was 6 mm diameter plastic particles.

Table 2. Physical robot characteristics.

Dimensions	$0.48 \times 0.028 \times 0.054 \text{ m}^3$
Mass	0.83 kg
Motor	HSR-5980SG
Motor torque	2.94 N m
Number of motors	6
Total segments	7

was 0.7 N m. To verify this finding we dragged an object with the same form factor as a motor through the 6 mm diameter plastic medium (see Table 1 for specifications) at 0.25 m s^{-1} . The measured force at a depth of 4 cm was 3.2 N. Since the maximum torque occurs at the middle motor (0.23 m to either end) we estimated the maximum possible total force along an effective segment extending from the middle servo to either the tail or the head (length 0.23 m) to be 18 N with a corresponding maximum torque of 4.0 N m. We selected a servomotor that exceeded both torque estimates, see Table 2.

Servomotors were powered in parallel from a 7.4 V, 30 A supply. The pulsewidth-based control signal for each motor was generated in LabVIEW using Equation (3) as a multiplexed signal, output from a PCI-card (NI-6230), and connected to the clock input of a decade counter (CD4017BC) which functions as a demultiplexer and distributes a control pulse to each motor every 20 ms.

Since the robot operates in granular media it is necessary to encase it in a material that prevents particles from getting between the motor segments but allows the device to undulate easily. After testing a number of materials we found that a two-layer encasement consisting of an outer

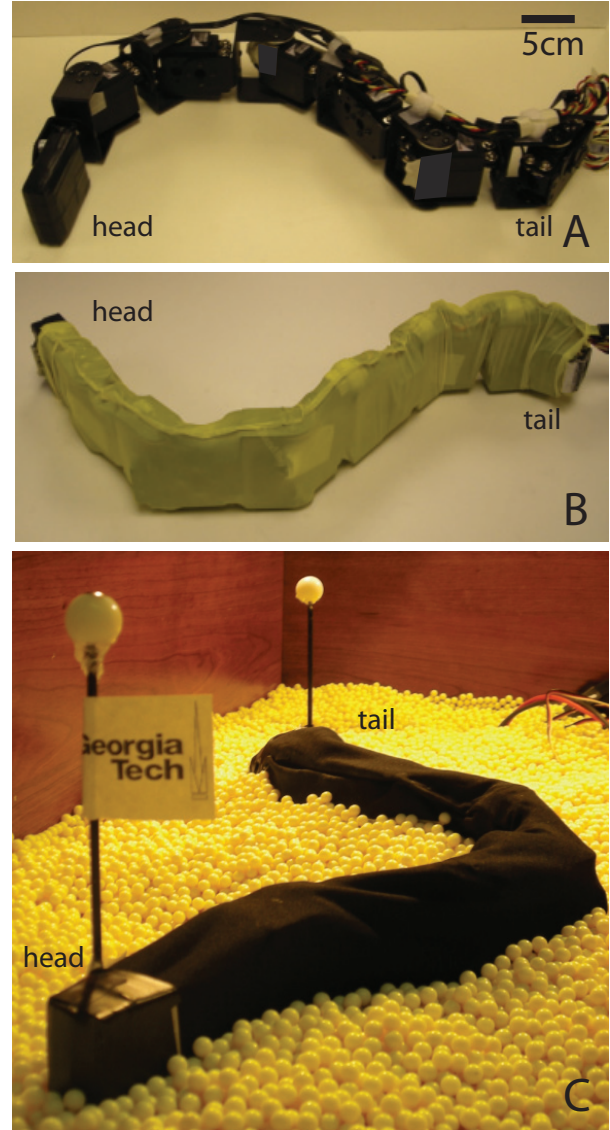


Fig. 5. The sand-swimming robot. (A) Basic construction (servomotors and aluminum brackets with power wires running along the top of the device). Robot has a double-layer skin: (B) tight fitting thin latex inner layer, and (C) Lycra spandex outer layer. Balls atop narrows masts on the head and tail segments facilitate subsurface motion tracking.

Lycra spandex sleeve with a single seam (located at the top of the device) enclosing an inner, thin latex sleeve that fit tautly around the motors was satisfactory (Figure 5).

4.2. Experimental methods

The robot was tested in a container with the same dimensions as used in the robot simulations and filled with 6 mm diameter plastic particles prepared in an as-poured state (Nedderman 1992). Overhead video (100 fps) was collected for each condition tested. To facilitate subsurface tracking, the first and last modules are fixed with a mast with a visible

marker at the top. The wire bundle is run up the mast on the last segment and tethered above the container. The kinematics of the subsurface motion of the robot were also obtained using X-ray imaging for a representative condition ($f = 0.25$ Hz, $A/\lambda = 0.2$), see Figure 6A–C. For each test the top of the robot was submerged 4 cm below the surface and the surface leveled. Owing to the servomotor velocity limits the maximum oscillation frequency was 1 Hz. For each frequency, data was collected for one or two motion cycles.

4.3. Results

To calibrate the device we placed it on a rigid surface and used video to track the position of the segments from which we determined the mapping between the maximum relative segment angle β_0 (Equation 3) and A/λ . Within the granular material the kinematics of the robot in experiment and simulation were similar (Figure 7). The forward velocity of the device increased monotonically with increasing oscillation frequency (Figure 4) for $A/\lambda = 0.2$ and a single period wave. The slope of this relationship (η) was 0.34 ± 0.02 . For the same parameters the simulation predicted $\eta = 0.36 \pm 0.02$ (within 8% of experiment).

The performance of a sand-swimmer is dependent on the thrust and drag forces generated by the body. Both forces are sensitive to particle–particle friction μ_{pp} and body–particle friction μ_{bp} (Maladen et al. 2009). We tested the swimming ability of the robot within poppy seeds (≈ 1 mm diameter) which we experimentally measured to have poppy seed–poppy seed μ_{pp} and poppy seed–robot skin μ_{bp} friction equal to 0.46 and 0.55, respectively. We found that the robot swims subsurface with $\eta = 0.34 \pm 0.01$, the same wave efficiency as measured within 6 mm diameter plastic particles ($\mu_{pp} = 0.08$ and $\mu_{bp} = 0.27$).

We used our numerical robot simulation to explain this result by investigating the effect of varying each friction coefficient (μ_{pp} and μ_{bp}) (while keeping the other fixed) on η . To reduce the computational time associated with simulating poppy seeds (nearly eight times more particles for the same container size as used in experiment) we tested the friction effect by varying the friction of the 6 mm particles (see Figure 8). We found that as expected due to the increased drag force, η of the simulated sandfish decreased with increasing μ_{bp} . Here η for the robot increased with increasing μ_{pp} because the yield stress of the media and the forces generated during continuous yielding were higher due to the higher friction; therefore larger thrust forces could be generated. For the condition when both μ_{bp} and μ_{pp} were simultaneously high or low there was no net effect on η , in accord with η measured for the robot swimming within poppy seeds for which both μ_{bp} and μ_{pp} were high.

5. Discussion

Like the sandfish, the robot swims within granular media by propagating a traveling sinusoidal wave posteriorly from

head to tail without limb use. The robot demonstrates subsurface locomotion in granular media using a relatively low degree of freedom device and an open-loop control scheme.

The robot however did not move forward as fast or with the same wave efficiency as the animal. In the biological experiments, η was approximately 0.5 for a range of granular material preparations and particle size. The robot in both experiment and simulation performed below this value. We hypothesized that the number of segments (for a fixed length device) affects both η and the forward speed of the device. Increasing the number of segments in the robot simulation showed the device moved forward faster and with greater wave efficiency until $N \approx 15$ where η plateaued (Figure 9). Interestingly, the maximum $\eta \approx 0.5$ was the same as measured in the animal experiment. We utilized our previously developed RFT to predict the performance of the sand-swimming device with parameters set to match those for the plastic particles used in the robot experiment. We estimated $\eta = 0.56$ for a smooth profiled undulator which is close to the numerical robot simulation prediction for $N > 15$ (gray band, Figure 9).

Increasing N allows the device to better match a sinusoidal wave profile and increases η . This suggests that deviations from the smooth form of a traveling sinusoidal wave reduces performance. A seven-segment robot operates below the minimum N required to achieve the maximum η . As a design criterion, N is important when the length of the device is fixed as increasing the number of motors beyond the minimum N (that maximizes η for a given robot configuration) requires motors with smaller dimensions but capable of producing the same torque and also provides no further improvement in η .

We calculated the time-varying torque generated by each actuated motor by summing the torque along the length of the segments actuated by it. As expected, the torque was sinusoidal for all motors and the torque amplitude generated by the central motors (3 and 4) was larger than the torque from the motors nearest the ends, see Figure 10. As noted earlier the maximum torque in the simulation of 0.7 N m was well below the maximum of the motors used in experiment (see Table 2). This ensured that the motors of the robot were able to generate the torque required to achieve the prescribed angular trajectories. Also, the fluctuations in torque at frequencies higher than the oscillation frequency of the robot were small in comparison to the torque amplitude.

The magnitude of the torque generated by each motor depended on its location along the robot (see Figure 10). We also varied the oscillation frequency of the simulated robot and found that the torques generated by the motors were independent of forward swimming velocity. This result supports our hypothesis that to a swimmer, a granular media behaves like a ‘frictional fluid’ where forces are generated by frictional contacts between the swimmer and the flowing particles and between the particles themselves. In such cases these frictional forces dominate the inertial forces and so the thrust and drag forces are largely speed

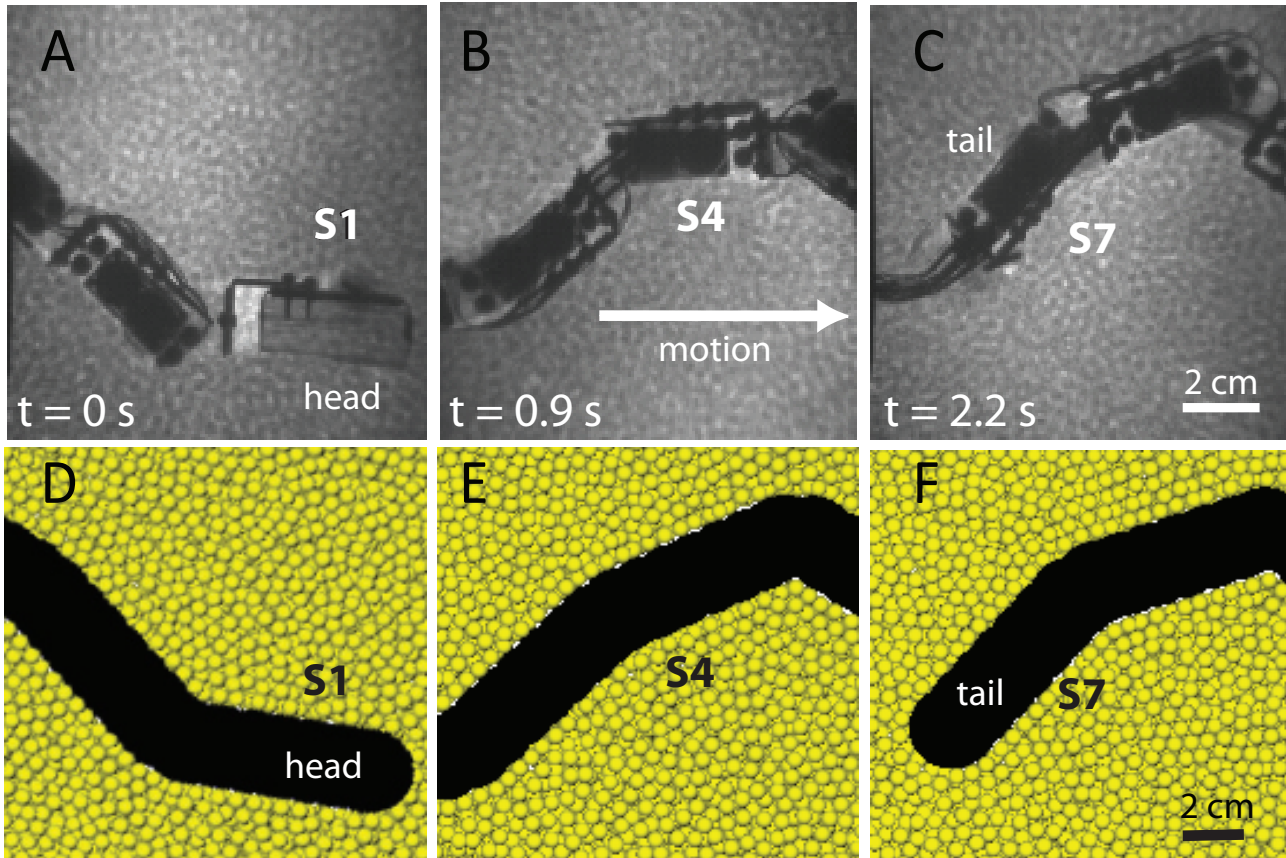


Fig. 6. Subsurface swimming in experiment and simulation. (A)–(C) Sequential X-ray images of the robot swimming in 6 mm particles, and (D)–(F) robot swimming in simulation. Segments from head to tail are denoted as S1 to S7. The oscillation frequency of both the physical and simulated robot is 1 Hz.

independent (Maladen et al. 2009). We had also shown previously that forces generated by dragging a rod within granular material (0.3 mm diameter glass particles) are speed independent in the regime of interest ($< 40 \text{ cm s}^{-1}$) (Maladen et al. 2009). As compared with the robot which moves in a non-inertial regime, an undulator moving within a low Reynolds (Re) number fluid experiences a viscous drag force (and torque) that varies linearly with the velocity (and oscillation frequency) (Purcell 1977) (see Figure 11). This result is significant as it reveals that the power (product of force and velocity) required to move within granular material scales linearly with velocity, while for non-inertial swimming within low Reynolds number fluids this relation is quadratic.

In addition to our subsurface studies, we tested whether the robot could locomote on the surface. Since snake-like robots move on flat rigid surfaces by mimicking the anisotropy in the friction coefficients observed in real snakes (Hu et al. 2009), it was not surprising that we found our robot with its isotropic skin could not advance on a flat rigid surface (see Figure 12D–F). However, when the robot was placed on the surface of the 6 mm diameter plastic particles used in the subsurface experiments, it moved forward

(see Figure 12A–C). The forward speed of the robot on the surface of 6 mm diameter plastic particles increased with increasing oscillation frequency. The wave efficiency η was 0.39 ± 0.02 (see Figure 4), nearly the same as that of the physical and simulated robot subsurface.

We tested the surface locomotion of the robot on poppy seeds to investigate the effect of particle friction (higher friction than 6 mm diameter plastic particles). When placed on the surface of a level bed of poppy seeds we found that the robot moved forward with low η (≈ 0.1) (see Figure 12G). As the robot was submerged to different initial depths (less than its height) it moved forward with an initially larger η (first half cycle) which as the robot rose upward, rapidly decreased to the smaller value of η observed for the robot placed on the surface.

The surface performance of the robot on poppy seeds was thus lower than its below surface performance; this was unlike the surface and below-surface performance in plastic particles, which was nearly identical. We observed that on the surface more material flowed back toward the robot as it undulated for the 6 mm diameter plastic particles than for the poppy seeds. This re-flow provided the robot material to push off from as it progressed forward.

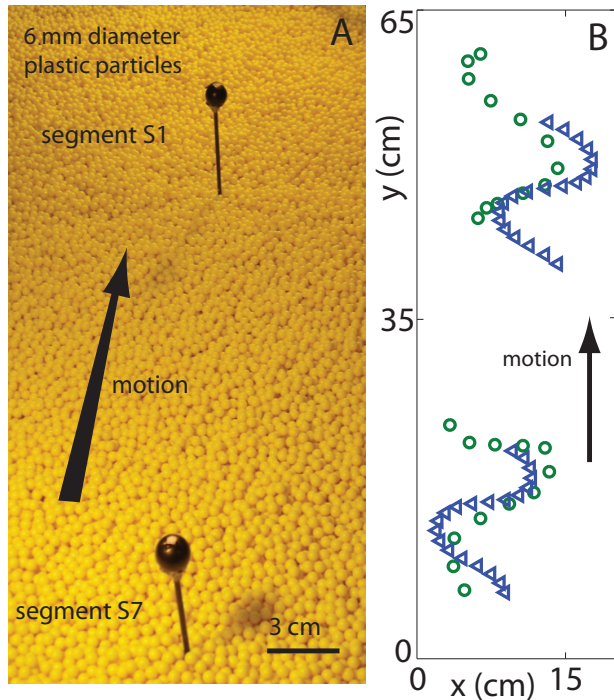


Fig. 7. Subsurface swimming in experiment and simulation. (A) Robot submerged in a container filled with 6 mm diameter plastic particles. Masts with spherical markers are attached to the first and last module. (B) Kinematics of the first and last segment of the robot tracked in experiment (green circles) and simulation (blue triangles).

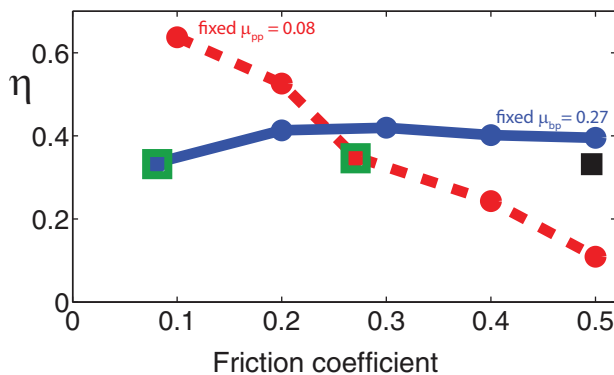


Fig. 8. Effect of friction on subsurface sand-swimming performance η of the simulated robot. η of the simulated robot in 6 mm diameter plastic particles for varying body-particle friction coefficient with constant $\mu_{pp} = 0.08$ (red dashed trace, open circles), and particle-particle friction coefficient with constant $\mu_{bp} = 0.27$ (blue solid trace, filled circles). Green open and black filled squares show η for the physical robot in 6 mm diameter plastic particles and ≈ 1 mm poppy seeds, respectively.

However, when the robot undulates subsurface, material refills from both the sides and above, and thus always provides the robot with material to push against. The angle

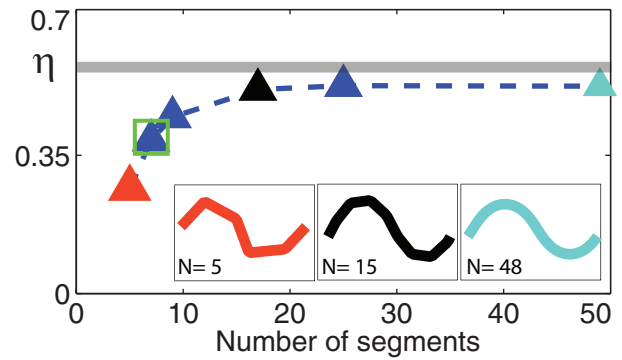


Fig. 9. Effect of the number of segments for fixed robot length on η from simulation (blue dashed curve with colored triangles, $f = 1$ Hz, and $A/\lambda = 0.2$). The red, black, and cyan triangles correspond to 5, 15, and 48 segment robots, respectively. The green square corresponds to the number of segments used in the physical robot, and the gray horizontal bar indicates η predicted by the RFT for a continuous body profile (see the text for details).

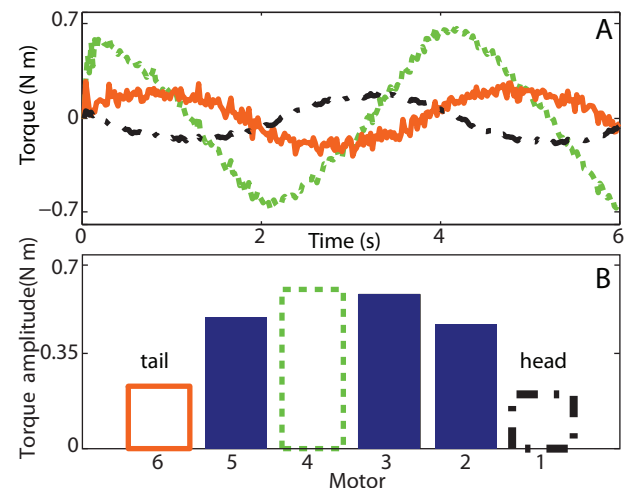


Fig. 10. Motor torque for the simulated seven-segment, six-motor robot ($f = 1$ Hz) (A) varying with time. (B) Torque amplitude versus motor position; orange (solid curve), green (dotted curve), and black (dash-dot curve) correspond to motors 6 (tail), 4, and 1 (head) with motor position 1 denoting segment number 2 in Figures 6 and 7.

of repose for the plastic particles (21°) is lower than the poppy seeds (30°) (see Figure 12G inset). This suggests that more material can pile up along the edge of the area swept out as the robot undulates for the higher friction poppy seeds than the 6 mm diameter plastic particles and results in a lower amount of re-flow as the robot undulates.

The results of the surface experiments show that on the surface of deformable media, undulators (including snakes (Gray 1946), nematodes (Gray and Lissmann 1964), and the robot) utilize the resistive force generated by pushing

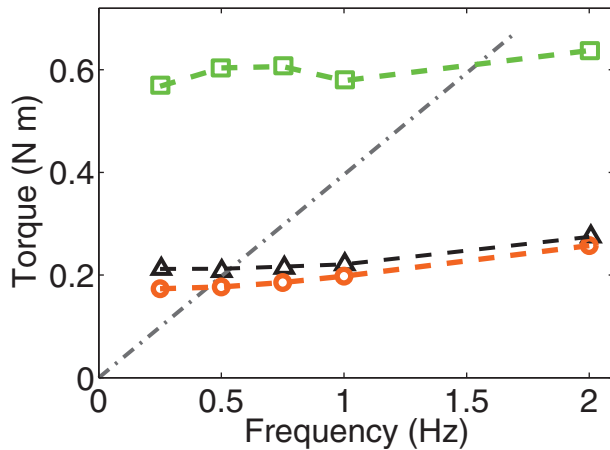


Fig. 11. Motor torque for the different segments of the simulated robot as a function of oscillation frequency. Orange (circles), green (squares), and black (triangles) dashed lines correspond to motors 6 (tail), 4, and 1 (head) with motor position 1 denoting segment number 2 in Figures 6, 7, and 10. Grey dash-dotted line corresponds to the functional form (linear relation) of the torque that would be experienced by the robot in a low Reynolds number fluid (Purcell 1977).

their body laterally against the medium to generate thrust and move forward. In this case the motion is not driven by the anisotropy in the friction coefficients of the interacting surfaces alone (which is the case for snakes and a number of snake robots on rigid surfaces). In contrast to the robot, however, η for snakes moving on the surface of deformable media is closer to 0.9 (Hu et al. 2009). This may be because the mechanics of a snake are more complicated than the simple planar gait of our robot. As a snake undulates laterally to progress forward its entire body is not in simultaneous contact with the media. Instead it lifts parts of its body and maintains contact at only a few points which reduces drag.

6. Future work

A sand-swimming robot combined with a validated simulation tool opens many avenues for further research. The sandfish lizard uses the same kinematics to move in a variety of media. We recently used our complementary theoretical, numerical, and physical modeling approaches to reveal that the kinematics used by the animal maximizes forward sand-swimming speed (Maladen et al. 2011). Of immediate interest would be to test the effect of the optimal kinematics on the mechanical cost of transport. Such discoveries coupled with the understanding obtained by targeting the animal's control methods and sensing modalities could lead to the development of a more effective sand-swimming robot. We also intend to develop feedback approaches similar to those used by snake (Hirose

et al. 1993) and salamander (Ijspeert et al. 2007) robots for moving within fluids and on various terrestrial substrates.

The shape of the sandfish suggests morphological adaptations that could aid in subsurface locomotion and these could be tested in the robot. For example, the cross-sectional shape of the sandfish (flat belly and rounded top) has been hypothesized to aid rapid burial into granular media (Mosauer 1932). The simulated and physical robots can be used to explore the influence of this morphology along with body taper on performance. The robotic simulation can also tune parameters such as skin friction and body compliance to identify optimal values which could then be tested with our physical device.

The results of the surface experiments reveal that the performance of a robot on the surface of granular media is different from that on a rigid surface and is a function of media properties such as friction. Further work is needed to investigate the effect of parameters such as the depth of burial (less than robot height), and media preparation (loosely or tightly packed) on surface performance. Insight into the mechanisms of force production while moving on the surface of granular media can be obtained by developing an empirical RFT similar to that presented in Maladen et al. (2009). The simulation and robotic tools developed in this paper can be used to answer questions related surface locomotion such as locomotor-media interaction (force and velocity fields), effect of number of segments on performance, cost of transport, and parameters affecting transitions from surface to subsurface locomotion.

7. Conclusion

Motivated by biological experiments revealing rapid sand-swimming in the sandfish lizard, we used numerical simulations as a design tool to build an undulatory sand-swimming device. We employed our simulation to test whether a device with a finite number of segments (seven) could advance using an open-loop (traveling wave sinusoid) control scheme and calculated the motor torque requirements for the robot. We then built and tested a prototype of the device to validate the biological observations and the predictions from the RFT (Maladen et al. 2009) and simulations that limbless body undulations are sufficient to propel the robot forward. Our findings show that the device swims, and that it translates faster by increasing its oscillation frequency just as the sandfish does. We showed that undulatory locomotion performance on the surface of granular media is different from that on a flat rigid surface. We also showed that the difference in performance between the robot on the surface and within a granular medium varies with particle friction. The design tools (numerical model and robot) we developed can generate testable hypotheses of neuromechanical control (Nishikawa et al. 2007) that may lead to an improved understanding of how organisms exploit the solid- and fluid-like properties of granular

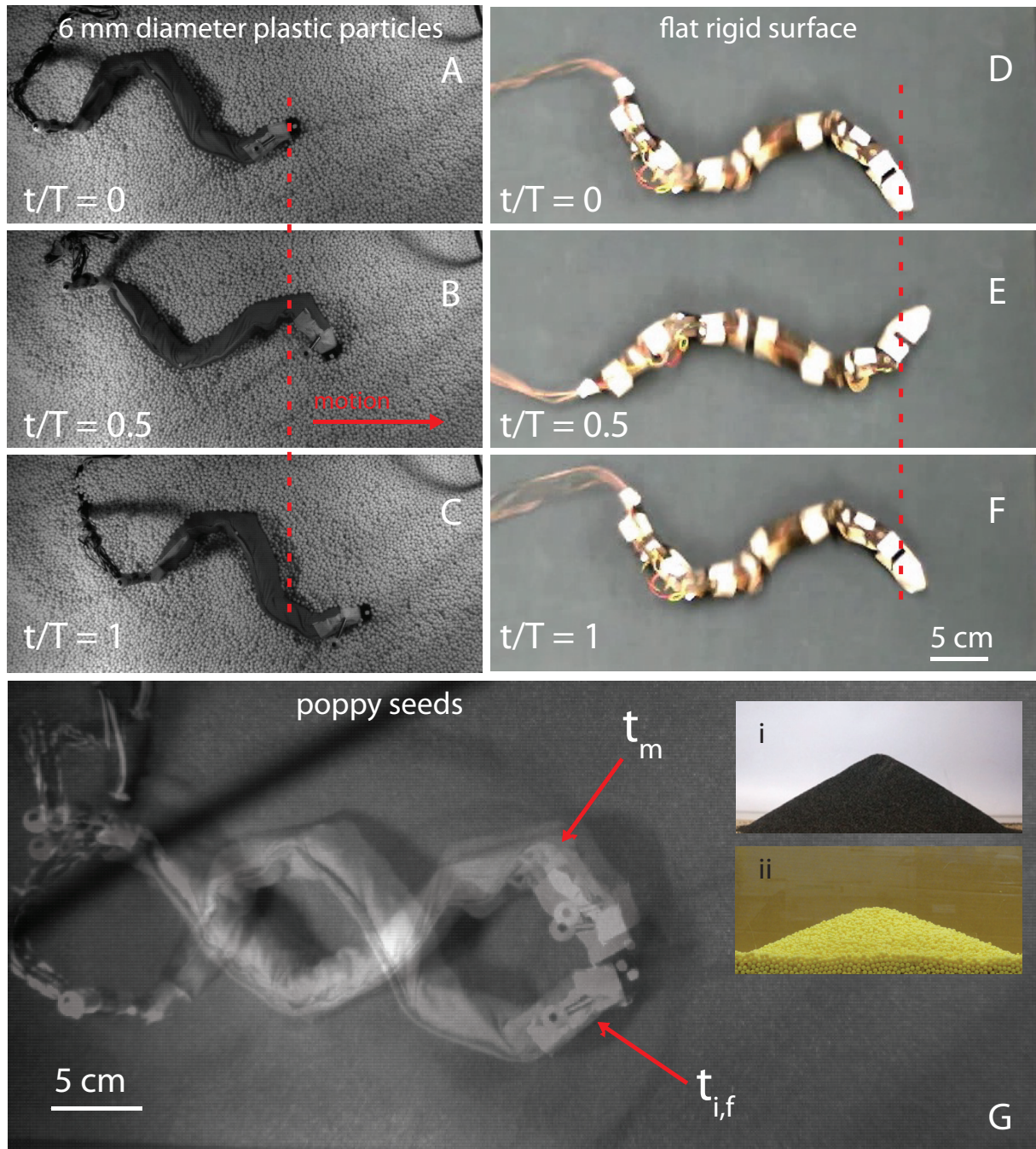


Fig. 12. Top view images of the robot tested on (A)–(C) the surface of the 6 mm diameter plastic particles, and (D)–(F) an isotropic flat Plexiglass sheet covered with a thin cotton fabric. Red dashed lines mark the initial position of the robot head, and highlight the forward progress made by the robot after one cycle of undulation. The base of the robot in (D)–(F) was covered with spandex material (the same as the robot outer casing for the subsurface experiments) and the edges of the material were taped to the side of the motors. (G) Overlaid images of the robot undulating on poppy seeds for one complete cycle. Here $t/T = 0$, $t/T = 0.5$, and $t/T = 1$ correspond to the beginning (t_i) middle (t_m), and end (t_f) of the cycle. Insets show the angle of repose of (i) the poppy seeds (30°), and (ii) the plastic particles (21°). The spatial and temporal parameters were kept fixed for both tests ($f = 0.5$ Hz).

media to move effectively within it. This will help create the next generation of biophysically inspired robots that can move on and within complex flowing environments.

Funding

This work was supported by the Burroughs Wellcome Fund Career Award at the Scientific Interface, NSF Physics of Living Systems

(grant number PHY-0749991), and the Army Research Laboratory (ARL) Micro Autonomous Systems and Technology (MAST) Collaborative Technology Alliance (CTA) (cooperative agreement number W911NF-08-2-0004).

Acknowledgments

We thank Dr David Hu for valuable discussions on snake locomotion. We thank Nick Gravish and Chen Li for help with drag experiments, and we thank Adam Kamor, Daniel Cohen and Andrew Slatton for assisting with the development of the numerical simulation.

References

- Arena P, Di Giamberardino P, Fortuna L, La Gala F, Monaco S, Muscato G, et al. (2004) Toward a mobile autonomous robotic system for Mars exploration. *Planetary and Space Science* 52: 23–30.
- Arnold E (1995) Identifying the effects of history on adaptation: origins of different sand-diving techniques in lizards. *Journal of Zoology, London* 235: 351–388.
- Ashcheulov A, Gutsul I and Maevski V (2000) Device for monitoring the radiation temperature in coal mines. *Journal of Optical Technology* 67(3): 281.
- Bagnold RA (1954) *The Physics of Blown Sand and Desert Dunes*. Methuen and Co. Ltd.
- Bekker M (1956) *Theory of Land Locomotion*. The University of Michigan Press.
- Berri S, Boyle J, Tassieri M, Hope I and Cohen N (2009) C. elegans locomotion: a unified multidisciplinary perspective. *BMC Neuroscience* 10(Suppl. 1): P16.
- Carranza S, Arnold E, Geniez P, Roca J and Mateo J (2008) Radiation, multiple dispersal and parallelism in the skinks, Chalcides and Sphenops (Squamata: Scincidae), with comments on Scincus and Scincopus and the age of the Sahara Desert. *Molecular Phylogenetics and Evolution* 46: 1071–1094.
- Chirikjian G and Burdick J (1995) The kinematics of hyper-redundant robot locomotion. *IEEE Transactions on Robotics and Automation* 11: 781–793.
- Choset H, Luntz J, Shammas E, Rached T, Hull D and Dent C (2000) Design and motion planning for serpentine robots. In *Proceedings of SPIE* 3990: 148.
- Cohen, N and Boyle, JH (2010) Swimming at low Reynolds number: a beginners guide to undulatory locomotion. *Contemporary Physics*, 51(2): pp. 103–123.
- Crespi A, Badertscher A, Guignard A and Ijspeert A (2005) Swimming and crawling with an amphibious snake robot. In *2005 IEEE International Conference on Robotics and Automation Proceedings*, Vol. 3, p. 3024.
- Desai R, Rosenberg C, Jones J and Inc I (1995) Kaa: an autonomous serpentine robot utilizes behavior control. In *1995 IEEE International Conference on Intelligent Robots and Systems Proceedings*.
- Ding Y, Gravish N and Goldman DI (2011) Drag induced lift in granular media. *Physical Review Letters* 106: 028001.
- Dorgan K, Arwade S and Jumars P (2007) Burrowing in marine muds by crack propagation: kinematics and forces. *Journal of Experimental Biology* 210: 4198.
- Dowling K (1999) Limbless locomotion: learning to crawl. In *1999 IEEE International Conference on Robotics and Automation Proceedings*, Vol. 4.
- Fielden L (1991) Home range and movement of the Namib Desert golden mole, *Eremitalpa granti namibensis* (Chrysochloridae). *Journal of Zoology* 223: 675–686.
- Gans C (1975) Tetrapod limblessness: evolution and functional corollaries. *Integrative and Comparative Biology* 15: 455.
- Gerritsen K, van den Bogert A and Nigg B (1995) Direct dynamics simulation of the impact phase in heel-toe running. *Journal of Biomechanics* 28: 661–668.
- Gillis G (1996) Undulatory locomotion in elongate aquatic vertebrates: Anguilliform swimming since Sir James Gray. *Integrative and Comparative Biology* 36: 656.
- Goldman D and Umbanhowar P (2008) Scaling and dynamics of sphere and disk impact into granular media. *Physical Review E* 77: 21308.
- Gray J (1946) The mechanism of locomotion in snakes. *Journal of Experimental Biology* 23: 101.
- Gray J and Hancock G (1955) The propulsion of sea-urchin spermatozoa. *Journal of Experimental Biology* 32: 802.
- Gray J and Lissmann H (1964) The locomotion of nematodes. *Journal of Experimental Biology* 41: 135.
- Hawke S and Farley R (1973) Ecology and behavior of the desert burrowing cockroach, *Arenivaga* sp. (Dictyoptera, Polyphagidae). *Oecologia* 11: 263–279.
- Hirose S, Cave P and Goulden C (1993) *Biologically Inspired Robots: Snake-like Locomotors and Manipulators*, Vol. 64. Oxford: Oxford University Press.
- Hirose S and Morishima A (1990) Design and control of a mobile robot with an articulated body. *The International Journal of Robotics Research* 9: 99.
- Hoover A, Steltz E and Fearing R (2008) RoACH: An autonomous 2.4 g crawling hexapod robot. In *2008 IEEE Intelligent Robots and Systems Proceedings*, pp. 26–33.
- Hopkins J, Spranklin B and Gupta S (2009) A survey of snake-inspired robot designs. *Bioinspiration and Biomimetics* 4: 021001.
- Hu D, Nirody J, Scott T and Shelley M (2009) The mechanics of slithering locomotion. *Proceedings of the National Academy of Sciences* 106(25): 10081.
- Humphrey C and Adams J (2009) Robotic tasks for chemical, biological, radiological, nuclear and explosive incident response. *Advanced Robotics* 23: 1217–1232.
- Ijspeert A, Crespi A, Ryzcko D and Cabelguyen J (2007) From swimming to walking with a salamander robot driven by a spinal cord model. *Science* 315: 1416.
- Jayne BC (1986) Kinematics of terrestrial snake locomotion. *Copeia* 4: 915–927.
- Kim H, Shim D and Sastry S (2002) Flying robots: modeling, control and decision making. In *2002 IEEE International Conference on Robotics and Automation Proceedings*, Vol. 1.
- Kim S, Clark JE and Cutkosky MR (2006) iSprawl: Design and tuning for high-speed autonomous open-loop running. *The International Journal of Robotics Research* 25: 903–912.
- Klaassen B and Paap K (1999) GMD-SNAKE 2: a snake-like robot driven by wheels and a method for motion control. In *1999 IEEE International Conference on Robotics and Automation Proceedings*, Vol. 4, pp. 3014–3019.
- Lee J and Herrmann H (1993) Angle of repose and angle of marginal stability: molecular dynamics of granular particles.

- Journal of Physics A: Mathematical and General* 26: 373–383.
- Li C, Umbanhowar PB, Komsuoglu H and Goldman DI (2010) The effect of limb kinematics on the speed of a legged robot on granular media. *Experimental Mechanics* 1–11.
- Li C, Umbanhowar PB, Komsuoglu H, Koditschek DE and Goldman DI (2009) Sensitive dependence of the motion of a legged robot on granular media. *Proceedings of the National Academy of Science of the USA* 106: 3029–3034.
- Maladen, RD, Ding, Y, Umbanhowar, PB, Kamor, A and Goldman, DI (2011). Mechanical models of sandfish locomotion reveal principles of high performance subsurface sand-swimming. *Journal of The Royal Society Interface*.
- Maladen R, Ding Y, Li C and Goldman D (2009) Undulatory swimming in sand: subsurface locomotion of the sandfish lizard. *Science* 325: 314.
- Maladen R, Umbanhowar P, Ding Y, Masse A and Goldman D (2011b) Lift control in a sand-swimming robot. In *2011 IEEE International Conference on Robotics and Automation Proceedings*.
- Marcus W, Legleiter C, Aspinall R, Boardman J and Crabtree R (2003) High spatial resolution hyperspectral mapping of in-stream habitats, depths, and woody debris in mountain streams. *Geomorphology* 55: 363–380.
- McKean J, Buechel S and Gaydos L (1991) Remote sensing and landslide hazard assessment. *Photogrammetric Engineering and Remote Sensing* 57: 1185–1193.
- Metternicht G, Hurni L and Gogu R (2005) Remote sensing of landslides: An analysis of the potential contribution to geo-spatial systems for hazard assessment in mountainous environments. *Remote Sensing of Environment* 98: 284–303.
- Meysman F, Middelburg J and Heip C (2006) Bioturbation: a fresh look at Darwin's last idea. *Trends in Ecology and Evolution* 21: 688–695.
- Mosauer W (1932) Adaptive convergence in the sand reptiles of the Sahara and of California: a study in structure and behavior. *Copeia* 72–78.
- Mouazen A and Nemenyi M (1999) Tillage tool design by the finite element method: Part 1. finite element modelling of soil plastic behaviour. *Journal of Agricultural Engineering Research* 72: 37–51.
- Nedderman, R. (1992). *Statics and Kinematics of Granular Materials*. Cambridge: Cambridge University Press.
- Nishikawa K, Biewener AA, Aerts P, Ahn AN, Chiel HJ, Daley MA, et al. (2007) Neuromechanics: an integrative approach for understanding motor control. *Integrative and Comparative Biology* 47: 16–54.
- Purcell, E.M. (1977) Life at low Reynolds number. *Am. J. Phys* 45(3): 11.
- Playter R, Buehler M and Raibert M (2006) Bigdog. In Grant DWG, Gerhart R and Shoemaker CM (eds), *Unmanned Ground Vehicle Technology VIII, Proceedings of SPIE* 6230: 62302O1–62302O6.
- Pica Ciamarra, M. and Lara, A.H. and Lee, A.T. and Goldman, D.I. and Vishik, I. and Swinney, H.L. (2004) Dynamics of drag and force distributions for projectile impact in a granular medium. *Physical review letters* 92(19): 194–301.
- Rapaport DC (2004) *The Art of Molecular Dynamics Simulation*, 2nd edition. Cambridge: Cambridge University Press.
- Ritzmann R, Quinn R and Fischer M (2004) Convergent evolution and locomotion through complex terrain by insects, vertebrates and robots. *Arthropod Structure and Development* 33: 361–379.
- Saranli U, Buehler M and Koditschek D (2001) Rhex: A simple and highly mobile hexapod robot. *The International Journal of Robotics Research* 20: 616.
- Silbert, L.E. and Ertaş, D. and Grest, G.S. and Halsey, T.C. and Levine, D. and Plimpton, S.J. (2001) Granular flow down an inclined plane: Bagnold scaling and rheology. *Physical Review E* 64(5): 051–302.
- Saunders A, Goldman DI, Full RJ and Buehler M (2006) The rise climbing robot: body and leg design. In Gerhart GR, Shoemaker CM and Gage DW (eds), *Unmanned Systems Technology VIII. Proceedings of SPIE* 6230: 623017.
- Seymour R, Withers P and Weathers W (2001) Energetics of burrowing, running, and free-living in the Namib Desert golden mole (*Eremitalpa namibensis*). *Journal of Zoology* 244: 107–117.
- Shan Y and Koren Y (1993) Obstacle accommodation motion planning. In *1993 IEEE Intelligent Autonomous Systems Proceedings*, p. 94.
- Siegwart R, Lamon P, Estier T, Lauria M and Piguët R (2002) Innovative design for wheeled locomotion in rough terrain. *Robotics and Autonomous Systems* 40: 151–162.
- Tritton D (1989) *Physical Fluid Dynamics*. Oxford: Oxford University Press.
- White C (2003) The influence of foraging mode and arid adaptation on the basal metabolic rates of burrowing mammals. *Physiological and Biochemical Zoology* 76: 122–134.
- Wong J (1984) On the study of wheel–soil interaction. *Journal of Terramechanics* 21: 117–131.
- Zufferey J, Klaptocz A, Beyeler A, Nicoud J and Floreano D (2007) A 10-gram vision-based flying robot. *Advanced Robotics* 21: 1671–1684.